THE JOURNAL OF PHYSICAL CHEMISTRY C

Article

Cite This: J. Phys. Chem. C 2019, 123, 24890−24898

pubs.acs.org/JPCC

Influence of the Cation on the Surface Electronic Band Structure and Magnetic Properties of Mn:ZnS and Mn:CdS Quantum Dot Thin Films

Andrew J. Yost,[*,†] Thilini K. Ekanayaka,[‡] Gautam Gurung,[‡] Gaurab Rimal,[§] Sabit Horoz,[∥] Jinke Tang,[⊥] Tula Paudel,[‡] and TeYu Chien[⊥]

[†]Department of Physics, Oklahoma State University, Stillwater, Oklahoma 74075, USA

[‡]Department of Physics and Astronomy, University of Nebraska−Lincoln, Lincoln, Nebraska 68588-0299, USA

[§]Department of Physics, Rutgers University, Piscataway, New Jersey 08854 USA

[∥]Department of Electrical and Electronics Engineering, Siirt University, Siirt 56100, Turkey

[⊥]Department of Physics and Astronomy, University of Wyoming, Laramie, Wyoming 82071, USA

Supporting Information

ABSTRACT: The effects of doping Mn into ZnS and CdS quantum dots (QDs) are reported. Scanning tunneling spectroscopy spectra show a reduction in the electronic band gap in both CdS and ZnS upon incorporation of the Mn dopant. Mn:ZnS exhibits a rigid band shift toward higher bias, which is reminiscent of a hole-doping effect. This rigid band shift in Mn:ZnS is argued, with the help of X-ray photoelectron spectroscopy, to be due to a hole-doping mechanism caused by the favorable formation of Zn vacancies and a reduction in S vacancies compared to that in undoped ZnS films. In CdS, no rigid band shift is observed even though the presence of Cd vacancies can be confirmed by photoemission and magnetic measurements. A strong sp−d hybridization is observed in the Mn:CdS film upon introduction of the Mn dopant. d^0 ferromagnetism is observed in both undoped ZnS and CdS QD thin films at room temperature. Upon doping of Mn into ZnS, the magnetization is reduced, suggesting an antiparallel alignment of Mn−Mn or Mn−Zn vacancy nearest neighbors. Density functional theory supports the experimental results, indicating that the nearest-neighbor Mn atoms prefer antiparallel alignment of their magnetic moments with preferred ground state of Mn in a +3 oxidation state.

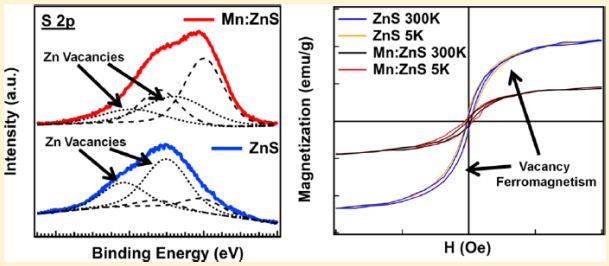

INTRODUCTION

Semiconducting quantum dots (QDs) are viable materials for next-generation solar cells as they have size-dependent optical and electronic properties because of quantum confinement, effectively allowing for variability of the optical and electronic band gaps.[1−3] Transition-metal doping in solar cell materials is another useful method for tailoring the optical, electronic, and magnetic properties of QDs beyond just changing the size. Historically, pure semiconducting QDs are known to produce low device performance,[4,5] but recently, it was shown that transition-metal dopants, specifically Mn, can be used to improve the overall device performance[6−8] in QD-sensitized solar cells. Transition-metal-doped QD semiconductors fall under the category of dilute magnetic semiconductors (DMSs). DMSs have applications in many fields and are important materials in the study of the magnetic dopants and their interactions with nonmagnetic electrons.[9−14] Bulk DMS materials are well studied, but the interaction of the magnetic electrons with nonmagnetic electrons is not well understood. Moreover, nanostructured DMSs are not well studied and even less understood compared to their bulk counterparts. Complicated phenomena occur when introducing quantum confinement to a DMS system, partially due to reduced volume and increased wave function overlap of the magnetic dopants with atoms in the center versus atoms at the edges of the QDs. It was recently shown by Yost et al.[15] that the magnetic dopant environment, specifically the location within or near the surface of the material, is important and can dramatically influence the electronic properties of a material at the nanoscale. Developing a detailed-nanoscale understanding of the mechanism by which the transition-metal dopant influences the electronic band structure is vital for obtaining precise doping control and desired material properties.

For decades, physicists, chemists, and engineers have been trying to fabricate better solar cells and other electronic devices through device-by-design schemes. The question arises: How

Received: July 10, 2019
Revised: September 16, 2019
Published: September 17, 2019

DOI: 10.1021/acs.jpcc.9b06551
J. Phys. Chem. C 2019, 123, 24890−24898

to generalize this procedure in order to design better materials for better devices? The key lies in a better understanding of the electronic structure, especially at the nanoscale, of material surfaces and interfaces. In any electronic device, there exists an interface between two materials. It is at this interface where physical phenomena occur and allow the device to operate and perform desired tasks. The way in which this interface comes into existence is very important and will determine the overall performance of the said device. Before the interface can come into existence, a surface of one of the two constituent materials must be established. Thus, investigating and understanding the nanoscale properties of the surfaces which will combine to form an interface and hence a device are fundamental to better device-by-design schemes.

In this study, we investigate the influence of Mn dopants on the surface electronic band structure and bulk magnetic properties of ZnS and CdS QDs using scanning tunneling spectroscopy (STS), X-ray photoemission spectroscopy, magnetic measurements, and density functional theory (DFT).

METHODS

ZnS and CdS samples were prepared using a wet chemical method whereby zinc acetate dihydrate, $Zn(CH_3COO)_2{\cdot}2H_2O$ 99.999% trace metals basis, or cadmium acetate tetrahydrate, $Cd(CH_3COO)_2{\cdot}2H_2O$ 99.995% trace metals basis (0.8662 g), was mixed with 40 mL of dimethyl sulfoxide (DMSO), $(CH_3)_2SO \geq 99.9\%$, which was then heated to around 65 °C under constant stirring; once at temperature, a solution of sodium sulfide, Na_2S (0.1561 g), in 10 mL of deionized water was injected into the Zn acetate/DMSO solution and heated for 9 h under constant stirring. In order to precipitate out the QDs, a ratio of 1:6 mL of unprecipitated solution to acetone, $CH_3COCH_3 \geq 99.9\%$, was used. The resulting powders were rinsed and centrifuged separately with methanol, $CH_3OH \geq 99.9\%$, and then isopropanol, $C_3H_8O \geq 99.9\%$, three times each in order to sufficiently remove any unreacted precursors. Following the rinsing step, the powders were mixed with isopropanol and drop-cast onto As:Si(100) substrates forming thick QD films. The Mn-doped materials were made with the same process described above by adding appropriate amounts (0.08662 g) of manganese acetate tetrahydrate, $Mn(CH_3COO)_2{\cdot}4H_2O$ 99.99% trace metals basis. X-ray photoemission spectroscopy indicates that the Mn:ZnS and Mn:CdS film surfaces contain roughly 5 ± 1 at. % Mn concentrations.

Scanning tunneling microscopy (STM) and STS were performed on an Omicron LT-STM at 77 K in a base pressure better than 1×10^{-11} mBar. X-ray photoelectron spectroscopy (XPS) was performed on a Kratos Axis Ultra X-ray photoelectron spectrometer, equipped with a monochromatic Al kα light source, at room temperature in a pressure better than 1×10^{-9} mBar. X-ray diffraction (XRD) was performed on a Rigaku SmartLab diffractometer at room temperature in air using a Cu kα X-ray source with a wavelength of 1.54 Å. Magnetic measurements were performed at 5 and 300 K in a Quantum Design PPMS system.

Computations were performed for a 64 atom, 2 × 2 × 2 supercell of the conventional zinc-blende cubic unit cell, with a Mn atom substituting one X atom in $X_{32}S_{32}$ (X = Zn, Cd). The ionic relaxation was done with spin polarization but without symmetry considerations until the Hellmann−Feynman forces were less than 0.01 eV/Å. A kinetic energy cutoff of 350 eV was used for the plane-wave expansion of the projector augmented waves[16] and 6 × 6 × 6 gamma-centered point grid of k points[17] for Brillouin zone integration. The nonisovalent Mn_X defect can have 0 and +1 ionization level. The ionized (charged) defect was created by adding or removing charge with a compensating jellium background. However, the charged supercell introduces two complications. The first is the interaction between the charge and its image. We take this into account by adding to the total energy, the screened Madelung energy of the point charge−image interaction in a lattice compensated by the jellium background, as suggested by Leslie and Gillan,[18] and the screened interaction between the delocalized part of the charge and its image because of Makov and Payne.[19] The dielectric constant that determines screening is calculated using density functional perturbation theory[20] as implemented in VASP. The second complication is the arbitrary shift in the total energy because of additional charge in the system. We correct this shift by calculating a difference in the atomic-sphere-averaged electrostatic potentials between the host and charged system.[21] These corrections effectively remove the supercell size-dependent energy of a charged system[22] and effectively represent the energy of an infinite crystal with a single charge (dilute limit), even for the smaller computation cell. To estimate the tendency of defect ionization, we calculate the charge transition energy $E(0/1^+)$ by taking the formation-energy difference, HF(0) − HF(+1). The formation energy is calculated using $HF(Mn_X,q) = E(Mn_X,q) - E_H + \mu_X - \mu_{Mn} + q(E_F + E_V)$, where $E(Mn_X,q)$ and E_H are the energy of the $X_{32}S_{32}$ (X = Zn, Cd) Mn-doped and updoped supercells, respectively, E_F is the Fermi energy, μ's are the chemical potential, and E_V is the valence band maximum (VBM). This approach assumes the chemical and charge equilibrium between the host and the atomic and charge reservoirs.[23]

RESULTS AND DISCUSSION

Crystal Structure of Mn-Doped and Undoped ZnS and CdS QD Thin Films. XRD was implemented to investigate the crystal structure of Mn-doped and undoped ZnS and CdS QD thin films. As indicated in the XRD profiles shown in Figure 1a, diffraction peaks corresponding to the ZnS(111), (220), and (311) crystal planes were observed for both ZnS and Mn:ZnS. Similarly, in Figure 1b, diffraction peaks corresponding to the CdS(111), (220), and (311) crystal planes were observed for both CdS and Mn:CdS. For both undoped and doped systems in ZnS and CdS, the XRD profiles indicate that the QDs adopt a zinc-blende structure with broad peaks in agreement with the DB card number 06-001-0792 for ZnS and 15-10-454 for CdS. The broadness of the diffraction peaks is related to the particle size, and the (111) peaks for the doped and undoped ZnS and CdS systems were fit using a Lorentzian function as can be seen in the Supporting Information. From the Lorentzian function fittings, the full width at half-maximum (fwhm) of the (111) peaks was used in conjunction with the Debye−Scherrer equation to determine the particle size for each system.[24] It was determined that both the ZnS and Mn:ZnS QDs are 1.5 ± 1 nm, while the CdS and Mn:CdS QDs are 1.8 ± 1 nm. These QD sizes agree well with the sizes observed in STM topography, see Supporting Information. It is important to notice that upon introduction of the Mn dopant, the crystal structure, size, and lattice constants remain unchanged for both the ZnS and CdS systems. This implies that any changes in electronic properties will not be related to changes in structure, size, or lattice constants.

DOI: 10.1021/acs.jpcc.9b06551
J. Phys. Chem. C 2019, 123, 24890−24898

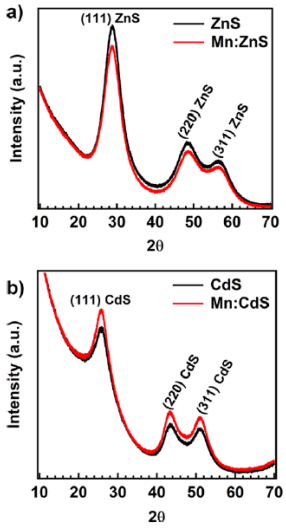

Figure 1. (a) XRD data for ZnS QDs (black) and Mn:ZnS QDs (red) showing a zinc-blende crystal structure. (b) XRD data for CdS QDs (black) and Mn:CdS QDs (red) showing a zinc-blende crystal structure.

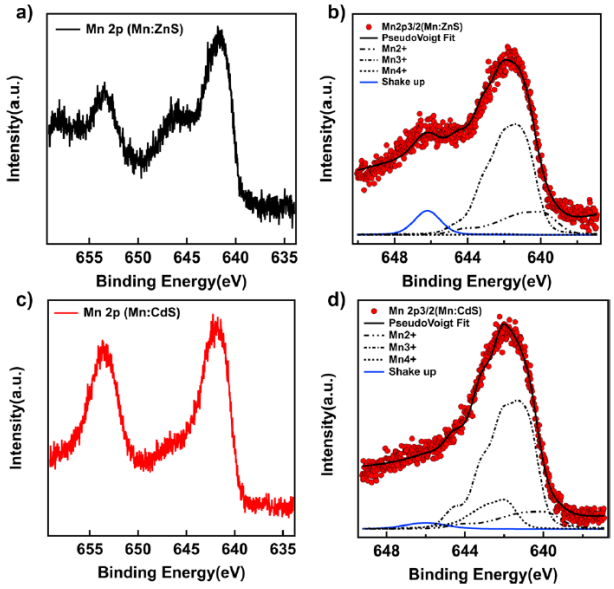

Figure 2. (a) XPS spectra for Mn 2p core-level features in Mn:ZnS QDs show the Mn $2p_{3/2}$ (lower binding energy) and Mn $2p_{1/2}$ (higher binding energy) features with associated shake-up peaks. (b) Mn $2p_{3/2}$ core-level feature with the shake-up peak (red dots) and pseudo-Voigt fit (black line), and below are the fitting curves of the envelope multiplet peaks for Mn +2, +3, and +4 (black dashed) along with the shake-up peak (blue). (c) XPS spectra for the Mn 2p core-level feature in Mn:CdS QDs show the Mn $2p_{3/2}$ (lower binding energy) and Mn $2p_{1/2}$ (higher binding energy) features with associated shake-up peaks. (d) Mn $2p_{3/2}$ core-level feature with the shake-up peak (red dots) and pseudo-Voigt fit (black line), and below are the fitting curves of the envelope multiplet peaks for Mn +2, +3, and +4 (black dashed) along with the shake-up peak (blue).

Surface Electronic Structure of Mn-Doped and Undoped ZnS and CdS QD Thin Films. The oxidation state of a dopant in a semiconducting material is fundamental in understanding the dopant's environment especially with respect to electron contribution and bonding in the material being doped. In Mn:ZnS and Mn:CdS, it is believed that Mn should replace the Zn^{2+} and Cd^{2+} ions during the synthesis process, which suggests that Mn should adopt a +2 oxidation state. The X-ray photoemission Mn 2p core-level features can be used to explore the final oxidation state for the Mn dopant near the surface in both Mn:ZnS and Mn:CdS QD thin films. A striking feature of the Mn $2p_{3/2}$ core-level photoemission feature, in both Mn:ZnS and Mn:CdS, is the broadness in the core-level peaks, as shown in Figure 2. The broadness can be quantified by the fwhm of the core-level features; in the case of both Mn:ZnS and Mn:CdS, the $2p_{3/2}$ fwhm is roughly 4 eV. As mentioned previously, it is expected that Mn is in a +2 oxidation state, which would result in a 2p core-level feature with peaks of fwhm < 2 eV and a higher binding energy satellite feature located at ~646 eV.[25,26] Broadening in photoemission core-level features can result from many complex phenomena, for example, surface-to-bulk core-level transitions,[27−30] multiplet splitting,[25,31] oxidation state change,[32−37] and screening effects[38−42] to name a few. For transition metals, especially Mn, it is well known that multiplet splitting occurs in the band structure.[25,26,31,35] Multiplet splitting occurs when an electron is excited from a deep energy level, and then an electron in a higher level interacts with the remaining unpaired electron in the deep level.[25,26] This interaction results in several higher energy final states which are observed in the XPS core-level spectra as a peak broadening at higher binding energy; thus, a larger fwhm is expected if multiplet splitting is present. Additionally, the presence of more than one oxidation state can lead to further broadening, which in fact is what is suggested by the XPS core-level features in Figure 2.

In order to confirm and quantify the presence of multiple oxidation states of the Mn dopant, both the Mn $2p_{3/2}$ and $2p_{1/2}$ core-level features are analyzed using a pseudo-Voigt fitting function. The fitting curves and data for Mn $2p_{3/2}$ core-level photoemission features in Mn:ZnS and Mn:CdS are shown in Figure 2b,d, respectively. The overall concentration of Mn in both the ZnS and CdS films is roughly 5 ± 1 at. %. The fitting curves and data for Mn $2p_{1/2}$ in Mn:ZnS and Mn:CdS are shown in the Supporting Information. In order to determine the relative concentrations of the Mn +2, +3, and +4 oxidation states from the XPS data, fitting parameters extracted from MnO, Mn_2O_3, and MnO_2 2p photoemission core-level features with contributions from multiplet splitting were used in the fitting procedure. Photoemission core-level features for MnO, Mn_2O_3, and MnO_2 represent pure oxidations states for Mn in the +2, +3, and +4 configurations and thus give a way to extract the different oxidation state contributions in the QDs. The multiplet peaks and the envelope fitting curves along with the multiplet peak position, relative peak intensities, and fwhm are shown in more detail in the Supporting Information. All parameters used for fitting the core-level features are the same as in the study by Nesbitt and Banerjee[25] for pure MnO, Mn_2O_3, and MnO_2 2p photoemission core-level features. As can be seen in Figure 2b,d, the fits agree well with the XPS data. It can be seen that there is a presence of all three oxidation states at the surface of both Mn:ZnS and Mn:CdS films, where the majority of Mn is in the +3 state. The intensities of the fitting peaks are used to determine the relative contributions of the Mn dopant in the +2, +3, and +4 oxidation states in the surface of the QD films. For Mn:ZnS, the relative Mn contributions as percentages of the overall Mn

DOI: 10.1021/acs.jpcc.9b06551
J. Phys. Chem. C 2019, 123, 24890−24898

concentration are as follows: Mn^{2+} = 20.6 ± 1%, Mn^{3+} = 79.0 ± 1%, and Mn^{4+} < 1%. The relative Mn contributions as percentages of the overall Mn concentration for Mn:CdS are as follows: Mn^{2+} = 12.7 ± 1%, Mn^{3+} = 73.0 ± 1%, and Mn^{4+} = 14.3 ± 1%. It is important to realize that XPS is able to probe the surface of the QD films and the relative contributions of oxidation states in the bulk of the films could be much different, and in fact, the amounts of Mn^{3+} and Mn^{4+} are probably much less percentages in the bulk of these films. Additionally, XPS indicates the presence of oxygen in the films (see the Supporting Information), but there is no indication that the oxygen is due to a Mn-oxide formation, rather it appears to be due to the presence of H_2O on the surface, SiO_2 in the substrate, and negligible amounts (<0.1%) of ZnO_2 or CdO_2 at the surface. A few questions, beyond the scope of the current study, arise concerning the hydroxylation/dehydroxylation of these OH species, which are as follows: "Can the OH species be removed upon annealing in vacuum or noble gas?" and "would prolonged exposure to ambient conditions influence the oxidation states of the Mn dopants?" Although we do not have current data which speak to these questions, the possibility of influencing the oxidation state through removal or addition of non-native species could have serious implications in material preparation and the subsequent device applications. These areas should be explored further in future experiments.

The presence of Mn at a higher than +2 oxidation state at the surface of the QD thin films is surprising given that there is no indication of Mn-oxide formation in the O 1s core-level photoemission spectra (see the Supporting Information) for both doped and undoped ZnS and CdS systems. A question arises: Are there sulfur vacancies or zinc (cadmium) vacancies present at the surface? Indeed, the XPS Zn 2p core-level spectra for undoped ZnS exhibit a peak asymmetry, not seen in Mn:ZnS, toward lower binding energy (see the Supporting Information), which represents Zn unbound to S, indicating that there are sulfur vacancies in the film surface. Additionally, the S 2p photoemission core-level features show a pronounced asymmetry toward higher binding energy in both Mn-doped and undoped ZnS, that is, S unbound to Zn, confirming the presence of Zn vacancies in the film surface. As determined from the compositional analysis of the S 2p core-level features, there are more than twice as many Zn vacancies present in the ZnS QD thin-film surfaces (>20 at. %) compared to that in the Mn:ZnS QD thin-film surfaces. The compositional analysis of the Zn 2p core-level features suggests that 8 ± 1 at. % of S vacancies exist in the undoped ZnS, whereas there were no observable S vacancies in the Mn:ZnS films.

On the other hand, the S 2p photoemission core-level features for the CdS systems exhibit a subtle broadening, indicating that CdS has less than 15 at. % Cd vacancies present near the surface, whereas Mn:CdS has less than 2 at. % Cd vacancies. The Cd 3d photoemission core-level features in doped and undoped CdS support the presence of a significant amount of S vacancies (>40 at. %), and in fact, this would require the film surface to behave as if metallic or at least very n-type, which is confirmed by STS as discussed below. Interestingly, the Cd 3d photoemission core-level feature for undoped CdS has three peaks, a shake-up peak at higher binding energy (~406 eV) (see the Supporting Information) compared to the peak because of unbound Cd at the surface, that is, sulfur vacancies (~404.5 eV) and the Cd^{2+} peak (405.1 eV). The shake-up peak does not appear in the Cd 3d spectrum for Mn-doped CdS, which exhibits a more metallic nature as seen in the dI/dV spectra discussed below. There are many governing phenomena which can appear as shake-up peaks in photoemission spectroscopy as previously mentioned. In the present case, there are three possible origins for the shake-up peak: (1) the presence of a surface plasmon, (2) peak broadening due to phonon excitations, that is, phonon broadening, and (3) a screened two-hole bound state. The plasmon energy, E_p, for Cd 3d is roughly $E_p \approx 9.2$ eV[43] and is thus too large to represent the energy shift of the shake-up peak, $\Delta E_{su} \approx 1.5$ eV, with respect to the peak because of the unbound Cd at the surface. Phonon broadening is not a likely origin as it is typically observed as energy shifts on the order of meV, $\Delta E_\delta < 1$ eV,[44−46] which is much smaller than $\Delta E_{su} \approx 1.5$ eV. A two-hole bound state occurs when photons excite a core electron, which leaves behind a core hole state. Then, the photoexcited electron experiences some kinetic energy loss, which is equivalent to the energy required to excite a valence electron to the conduction band, that is, the electronic band gap, E_g. The excited valence electron leaves behind a valence hole and hence the term two-hole bound state.[47] Thus, for an unscreened photoelectron, ΔE_{su} would be equal to the band gap of the CdS QD thin films, $E_g \approx 2.6$ V, as determined by STS (discussed below) and a peak should appear ~2.6 eV higher in binding energy than the peak because of the unbound Cd at the surface. As ΔE_{su} is slightly less than E_g, this means that the ejected photoelectron has a slightly higher than expected kinetic energy (lower binding energy) because of a repulsive potential.[39] This would suggest that the core hole is being screened because of charge-transfer effects[39] and hence the term screened two-hole bound state, which can be used to explain why ΔE_{su} is slightly less than E_g. The two-hole bound state is not seen in the Cd 3d core-level features in Mn:CdS films as these films are even more n-type, one may even say metallic in nature, compared to that in the undoped CdS film (see Figure 3b and discussion below). A metallic system tends to quench the resonance and thus the emission of two-hole

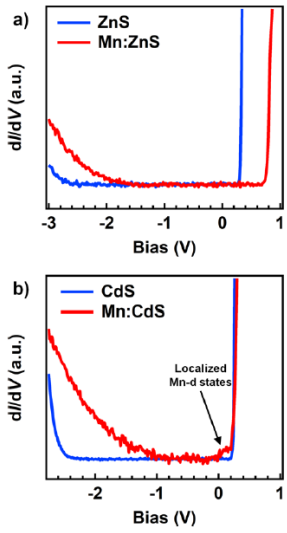

Figure 3. STS spectra for (a) ZnS QDs (blue) and Mn:ZnS QDs (red), setpoint = −3 V bias, 500 pA and for (b) CdS QDs (blue) and Mn:CdS QDs (red), setpoint = −3 V bias, 300 pA; black arrow emphasizes a localized in-gap feature because of Mn d states near the conduction band edge.

DOI: 10.1021/acs.jpcc.9b06551
J. Phys. Chem. C 2019, 123, 24890−24898

bound state transitions because of the presence of free electrons and the multitude of extremely fast decay routes, so the intensity of the photoemission signal is dramatically reduced.[48,49]

If there are any vacancies in the film surface, there should be a noticeable doping effect in the electronic band structure. For example, if sulfur vacancies are present in the film surface, this would lead to an excess of electrons, so it is reasonable to expect an electron-doping effect. This would cause the valence band and conduction band to rigidly shift toward lower energy with respect to the Fermi level. In other words, the valence (conduction) band would shift away (toward) from the Fermi level if an electron-doping effect occurs or equivalently, it could be said that the Fermi level would shift up away (toward) from the valence (conduction) band. A rigid band shift indicates that the band edges maintain the same relative shape, and thus, the density of states does not vary appreciably, rather the band edges shift along the energy axis. Thus, the presence of sulfur vacancies would require that the undoped and doped films be n-type in nature. On the other hand, if a significant presence of zinc (cadmium) vacancies is in the surface of the films, then an excess of holes would lead to a hole-doping effect. In the case of hole doping, a rigid band shift toward higher energy with respect to the Fermi level is expected. Thus, the valence (conduction) band would shift toward (away from) the Fermi level. The doped and undoped films are expected to be p-type if there is a significant presence of zinc (cadmium) vacancies. Additionally, as ∼70−80% of the Mn dopants in Mn:ZnS and Mn:CdS are present in a higher oxidation state (+3), this suggests that Mn contributes extra electrons, so an electron-doping effect should occur in the Mn-doped samples as well.

In order to investigate the nature of the vacancies and their influence on the positions of the conduction and valence bands with respect to the Fermi level, STS was performed on both doped and undoped ZnS and CdS in QDs of roughly 1.5 nm in diameter. In STS, the Fermi level is fixed at zero bias, so the first thing to notice is that both Mn-doped and undoped ZnS and CdS appear to be n-type, as shown in Figure 3. The n-type nature of the undoped ZnS as measured by STS would appear to contradict the XPS data, which indicated a large presence of Zn vacancies (>20 at. %) as compared to sulfur vacancies (8 at. %) in the film surfaces, indicating that the films should be p-type. XPS is able to probe the first several atomic layers (<10 Å) of the film surface, whereas STS is only capable of measuring the top most layer of the film, which suggests that XPS is able to measure most of the bulk properties compared to STS. This implies that the surface as measured by STS is n-type, while the bulk layers beneath the topmost surface layer are p-type. This difference in doping between the bulk and the surface has been observed in other materials including hybrid halide perovskites.[50] Now, if we consider the effect of the band structure upon the incorporation of Mn for Mn:ZnS, as shown in Figure 3a, it is obvious that there is a rigid band shift toward higher bias reminiscent of a hole-doping effect. The valence and conduction band edges maintain the same relative shape, but there is a slight reduction in the band gap in Mn:ZnS compared to that in ZnS, suggesting weak sp−d hybridization between Mn and ZnS. This is slightly perplexing as an electron-doping effect should occur upon introduction of the Mn dopant, and thus, we should see a rigid shift in the opposite direction. The only way we can have a hole-doping effect is if the Mn:ZnS films have either more Zn vacancies and/or less S vacancies in comparison to the undoped ZnS film. XPS data indicated the latter, and no detectable sulfur vacancies were observed for the Mn:ZnS films.

In contrast to the ZnS system, the dI/dV spectra of Mn-doped and undoped CdS QD films, as shown in Figure 3b, do not indicate a rigid band shift upon Mn doping. Mn doping in CdS appears to cause a significant reduction in the band gap and induces mid-gap localized states near the conduction band edge. The mid-gap state is a small feature appearing around 0.0−0.2 V in the Mn:CdS dI/dV spectra (red curve) in Figure 3b emphasized by a black arrow. The band gap reduction for CdS is much more obvious than for ZnS, suggesting that the Mn incorporated into CdS may have a stronger interaction with the band electrons of CdS than with that of ZnS. Because of the absence of the rigid band shift in the dI/dV spectrum of Mn:CdS, hole doping cannot be used to explain the influence of Mn on the electronic band structure for CdS. Another mechanism must be dominating in order to cause a large reduction in band gap and induce mid-gap states. One possibility is the existence of a large exchange interaction caused by the Mn dopant with the Cd and S band electrons, that is, strong sp−d hybridization. Additionally, the extreme n-type band structure of the Mn-doped and undoped CdS QD films confirms that sulfur vacancies must be present and the surface is highly conducting as suggested above by XPS measurements. To explain the experimental results, we performed DFT (for details, see Methods) calculations including a Mn dopant in bulk ZnS and CdS (Figure 4a). Figure 4c,d shows the spin-resolved density of states of Mn-doped ZnS and CdS compared with that of the undoped samples, showing the presence of localized occupied states in the band gap, that is, mid-gap states, of both ZnS and CdS. This can be further seen from the defect charge density plot in Figure 4a, which shows that the defect state is well localized

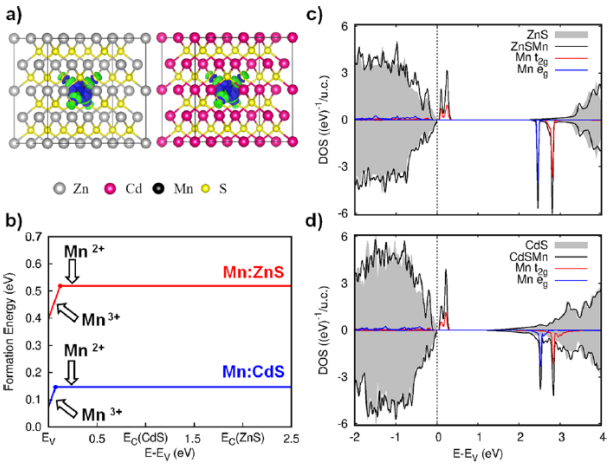

Figure 4. First principles defect calculations: (a) dopant Mn-induced localized charge density in ZnS and CdS. (b) Formation energy of charge neutral (M^{2+}, in line with the zero slope) and unit positive charged defect (Mn^{3+}, in line with the unit slope) plotted as a function of energy in the band gap of ZnS and CdS. At the VBM, the unit positive charged defect is energetically favorable. However, its formation energy increases with energy in band gap and loses its favorable status to neutral defect when the energy increases ∼0.2 eV above the VBM. The dot represents the energy position of charge transition (+1/0). (c,d) Density of states of the Mn-doped ZnS and CdS compared with the host unit cell showing deep defects in the band gap.

DOI: 10.1021/acs.jpcc.9b06551
J. Phys. Chem. C 2019, 123, 24890−24898

within the radial distance of the second nearest neighbor from the dopant atom. The localized nature of defects leads to deep charge transition levels, which are calculated by comparing the formation energy of a doped system in the presence of various amounts of charge. Figure 4b shows the formation energies of 0 and +1 charge states, which approximately represent the Mn^{2+} and Mn^{3+} oxidation states of a Mn dopant, respectively, in the band gap region of ZnS and CdS. In both compounds, the +1 charge state becomes a ground state for the p-type-like condition where the Fermi level moves closer to the VBM. This is consistent with the prevalence of Mn^{3+} states over Mn^{2+} and Mn^{4+} and the apparent increase in density of states at low bias (negative bias region in Figure 3), which resulted in the Fermi level shifting closer to the valence band edge as shown in Figure 3. Our model suggests that the increased dI/dV signal near the VBM of both the Mn-doped ZnS and CdS systems is due to contributions from a t_{2g} orbital of the split Mn d state and strong p−d hybridization. The Mn dopant itself, however, is not likely to be the source of the rigid shift observed in the STS curve as it cannot produce any hole contribution upon substituting for the Zn atom; thus, there may be a contribution from hole states because of Zn and Cd vacancy formation. The question arose: Can Mn dopants facilitate the formation of hole-producing defects, such as cation vacancies, by binding with them and lowering their formation energy? To investigate such a possibility, we calculated the formation energy of V_{Zn} in the presence and absence of a Mn dopant and found that the formation energy of V_{Zn} gets reduced by ~0.2 eV in the presence of a Mn dopant in ZnS. The formation of such defect complexes may dope the system with hole carriers, thereby shifting the Fermi level toward the valence band and stabilizing Mn^{3+} as found in the experiment.

Magnetic Properties of Mn-Doped and Undoped ZnS and CdS QD Thin Films. Vacancy-induced ferromagnetism is a common phenomenon appearing in a wide range of semiconducting materials such as ZnO,[51−53] C-implanted ZnO,[54] Mn:ZnO,[55,56] ZnS,[57] Mn:ZnS,[58] PbS,[59] TiO_2,[60,61] In_2O_3,[61] SnO_2,[62] and HfO_2.[61,63] In the interest of exploring the magnetic nature of the vacancies and Mn dopant, magnetization (M) versus applied magnetic field (H) was measured for each sample of the Mn-doped and undoped ZnS and CdS QD thin films at 5 and 300 K, as shown in Figure 5. At both 5 and 300 K, the undoped ZnS QD thin films exhibit a ferromagnetic hysteresis. Upon introduction of the Mn dopant, the magnetization reduces dramatically, as shown in Figure 5a, but the coercive field at 5 K increases by roughly 150% from 61 ± 4 Oe in the undoped ZnS to 152 ± 4 Oe in the Mn-doped ZnS QD thin films, as shown in Figure 5b. The reduced magnetization accompanied by the increased coercive field in Mn:ZnS is not unexpected as the magnetization is inversely proportional to the coercive field in magnetic systems with magnetic moments which are aligned parallel. In comparison to the ZnS systems, the Mn-doped and undoped CdS QD thin films both exhibit ferromagnetism at 5 and 300 K as shown in Figure 5c; however, there is no significant change to the magnetization upon introduction of the Mn dopant. The coercive field at 5 K, in contrast with the ZnS system, decreases slightly by roughly 4% from 124 ± 5 Oe in the undoped CdS to 119 ± 5 Oe in the Mn:CdS QD thin films, as shown in Figure 5d. Additionally, the coercive field at 300 K reduces by almost 27% upon incorporation of the Mn dopant into CdS.

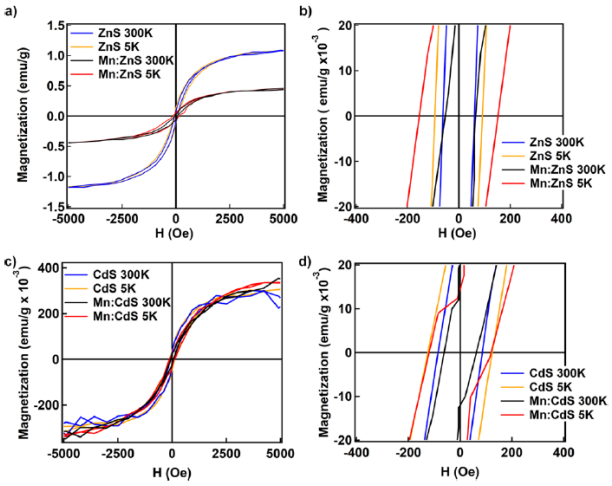

Figure 5. Magnetization (M) vs applied magnetic field (H) at 5 and 300 K for (a) ZnS and Mn:ZnS QD thin films, (b) zoomed-in image of (a) showing the coercive fields and for (c) CdS and Mn:CdS QD thin films, (d) zoomed-in image of (c) showing the coercive fields.

The ferromagnetic hysteresis in both the Mn-doped and undoped ZnS and CdS systems is due to the presence of Zn (Cd) vacancies rather than S vacancies as has been shown in the literature.[57,64,65] The reduced magnetization of the doped ZnS system suggests that the Mn dopant, by replacing the Zn atoms, reduces the overall ferromagnetic behavior of the samples. This is surprising given that Mn has a rather large effective magnetic moment, μ_{eff}, as compared to the effective magnetic moment of Zn vacancies as evidenced by the literature for Mn^{2+} μ_{eff} = 5.3−6.2 μ_B,[66,67] Mn^{3+} μ_{eff} = 4.8−4.9 μ_B,[67,68] and V_{Zn} μ_{eff} = 1.5−1.77 μ_B.[69−71] The calculations from the model in this study indicate a calculated local magnetic moment of the Mn dopant $\mu_{eff} \approx 4.2$ μ_B. The relatively large local moment can be explained based on crystal field theory in a tetrahedral environment and the large exchange splitting of the Mn atom. In the tetrahedral environment, dopant Mn d states split into e_g, nonbonding, and t_{2g}—p−d bonding orbitals, as shown in Figure 4c,d; the latter are at higher energy because of larger Coulomb repulsion along the bond direction. Because of even larger exchange splitting, orbitals of one spin channel become occupied before the other. This leads to dopant $e_g\uparrow$ and $t_{2g}\uparrow$ states being occupied, giving rise to a local moment of $\mu_{eff} \approx 4.2$ μ_B. Indeed, this large value of magnetic moment reinforces the concept of the localized nature of the defect state in bulk ZnS and CdS. Moreover, this suggests that the reduced magnetization upon introduction of large moment Mn ions is due to some exchange or alignment of the local magnetic moments, which is nonferromagnetic, possibly antiferromagnetic, or ferrimagnetic. This may exhibit itself as a possible antiparallel alignment of magnetic moments between Mn−Mn or Mn−Zn:vacancy nearest neighbors.

The alignment scheme of the magnetic moments can be determined through the calculated magnetic exchange terms by comparing the energy difference between ferromagnetically and antiferromagnetically coupled Mn substituting Zn in ZnS and Cd in CdS. The magnetic exchange term, J_{ij}, was determined, in a DFT calculation, to be antiferromagnetic regardless of separation between the magnetic ions, with the exchange energy decreasing exponentially with the separation distance between substituted Mn atoms. Additionally, the Mn

DOI: 10.1021/acs.jpcc.9b06551
J. Phys. Chem. C 2019, 123, 24890−24898

surface atoms, according to the calculations, would be antiferromagnetically coupled to the neighboring atoms beneath the surface and so on. As the ZnS and CdS systems are not layered materials, it is not expected that the Mn atoms in the surface are ferromagnetically ordered at the surface and antiferromagnetically coupled to the next Mn atoms beneath the surface. This antiferromagnetic type of exchange, present throughout the QD, is consistent with the experimental observation of reduced moments upon Mn doping in ZnS nanocrystals. The Zn and Cd vacancies at the surface have a larger presence (>15 at. %), when compared to Mn (5 at. %). As the cation vacancies are responsible for the ferromagnetism, it is reasonable to assume that the surface magnetization is mostly due to a strong ferromagnetic ordering between vacancies in close proximity. Further experiments with atomic spin resolution, such as spin-polarized STM, are required to explore the nature of the surface magnetic structure as related to the cation vacancies.

■ CONCLUSIONS

This study has shown that the surface electronic band structures of Mn-doped and undoped ZnS and CdS experience a reduction in band gap. The introduction of Mn dopants in ZnS QDs causes a rigid band shift in the electronic structure because of a hole-doping mechanism and favorable Zn vacancy formation. XPS core-level spectroscopy supports the hole-doping mechanism and indicates that at the surface the Mn dopant exists in a mostly +3 oxidation state in both doped ZnS and CdS QD thin films. Unlike in Mn:ZnS, Mn:CdS experiences no rigid band shift in the surface electronic structure even though Cd vacancies are present, indicating that the dominant influence on the band structure is due to strong sp−d hybridization. Magnetism measurements confirm the presence of Zn and Cd vacancies through the observation of d^0 ferromagnetism at both room temperature and 5 K. DFT indicates that the Mn nearest neighbors are antiferromagnetically aligned, which corroborates the reduced magnetization observed in the Mn:ZnS QD thin films. From this work, it can be understood that the oxidation state of the transition-metal dopant must be considered when tailoring the electronic band structure at the surface of a material and when creating interfaces for use in electronic devices.

■ ASSOCIATED CONTENT

Supporting Information

The Supporting Information is available free of charge on the ACS Publications website at DOI: 10.1021/acs.jpcc.9b06551.

STM topography images and XPS fitting parameters and other XPS data for Cd, Zn, and S core levels (PDF)

■ AUTHOR INFORMATION

Corresponding Author

*E-mail: andrew.yost@okstate.edu.

ORCID

TeYu Chien: 0000-0001-7133-6650

Notes

The authors declare no competing financial interest.

■ ACKNOWLEDGMENTS

This project was supported in part by the U.S. Department of Energy, Office of Basic Energy Sciences, Division of Materials Science and Engineering, DEFG02-10ER46728. This work was further supported by the National Science Foundation (DMR-1710512), the University of Wyoming EE-Nanotechnology Program Grant #0948027 (NSF-40243), and the Wyoming NASA Space Grant Consortium, NASA Grant #NNX15AI08H. Additional support was provided by the Nebraska Public Power District through the Nebraska Center for Energy Sciences Research at the University of Nebraska−Lincoln, NCESR grant number 19-SE-2018.

■ REFERENCES

(1) Wu, L.; Yu, J. C.; Fu, X. Characterization and Photocatalytic Mechanism of Nanosized CdS Coupled TiO2 Nanocrystals under Visible Light Irradiation. *J. Mol. Catal. A: Chem.* **2006**, *244*, 25−32.

(2) Singh, V.; Chauhan, P. Structural and Optical Characterization of CdS Nanoparticles Prepared by Chemical Precipitation Method. *J. Phys. Chem. Solids* **2009**, *70*, 1074−1079.

(3) Chatterjee, M.; Patra, a. Cadmium Sulfide Aggregates through Reverse Micelles. *J. Am. Ceram. Soc.* **2001**, *84*, 1439−1444.

(4) Diguna, L. J.; Shen, Q.; Kobayashi, J.; Toyoda, T. High Efficiency of CdSe Quantum-Dot-Sensitized TiO2 Inverse Opal Solar Cells. *Appl. Phys. Lett.* **2007**, *91*, 023116.

(5) Pattantyus-Abraham, A. G.; Kramer, I. J.; Barkhouse, A. R.; Wang, X.; Konstantatos, G.; Debnath, R.; Levina, L.; Raabe, I.; Nazeeruddin, M. K.; Grätzel, M.; et al. Depleted-Heterojunction Colloidal Quantum Dot Solar Cells. *ACS Nano* **2010**, *4*, 3374−3380.

(6) Rimal, G.; Pimachev, A. K.; Yost, A. J.; Poudyal, U.; Maloney, S.; Wang, W.; Chien, T.; Dahnovsky, Y.; Tang, J. Giant Photocurrent Enhancement by Transition Metal Doping in Quantum Dot Sensitized Solar Cells. *Appl. Phys. Lett.* **2016**, *109*, 103901.

(7) Horoz, S.; Dai, Q.; Maloney, F. S.; Yakami, B.; Pikal, J. M.; Zhang, X.; Wang, J.; Wang, W.; Tang, J. Absorption Induced by Mn Doping of ZnS for Improved Sensitized Quantum-Dot Solar Cells. *Phys. Rev. Appl.* **2015**, *3*, 024011.

(8) Dai, Q.; Sabio, E. M.; Wang, W.; Tang, J. Pulsed Laser Deposition of Mn Doped CdSe Quantum Dots for Improved Solar Cell Performance. *Appl. Phys. Lett.* **2014**, *104*, 183901.

(9) Tang, J.-M.; Flatté, M. E. Multiband Tight-Binding Model of Local Magnetism in Ga1-XMnxAs. *Phys. Rev. Lett.* **2004**, *92*, 047201.

(10) Munekata, H.; Ohno, H.; Von Molnar, S.; Segmüller, A.; Chang, L. L.; Esaki, L. Diluted Magnetic III-V Semiconductors. *Phys. Rev. Lett.* **1989**, *63*, 1849−1852.

(11) Ohno, H.; Munekata, H.; Penney, T.; von Molnár, S.; Chang, L. L. Magnetotransport Properties of P-Type (In,Mn) As Diluted Magnetic III-V Semiconductors. *Phys. Rev. Lett.* **1992**, *68*, 2664−2667.

(12) Medvedkin, G. A.; Ishibashi, T.; Nishi, T.; Hayata, K.; Hasegawa, Y.; Sato, K. Room Temperature Ferromagnetism in Novel Diluted Magnetic Semiconductor Cd1-XMnxGeP2. *Jpn. J. Appl. Phys.* **2000**, *39*, L949.

(13) Reed, M. L.; El-Masry, N. A.; Stadelmaier, H. H.; Ritums, M. K.; Reed, M. J.; Parker, C. A.; Roberts, J. C.; Bedair, S. M. Room Temperature Ferromagnetic Properties of (Ga, Mn)N. *Appl. Phys. Lett.* **2001**, *79*, 3473−3475.

(14) Sonoda, S.; Shimizu, S.; Sasaki, T.; Yamamoto, Y.; Hori, H. Molecular Beam Epitaxy of Wurtzite (Ga, Mn)N Films on Sapphire(0 0 0 1) Showing the Ferromagnetic Behaviour at Room Temperature. *J. Cryst. Growth* **2002**, *237−239*, 1358−1362.

(15) Yost, A. J.; Pimachev, A.; Rimal, G.; Tang, J.; Dahnovsky, Y.; Chien, T. Effects of Mn Dopant Locations on the Electronic Bandgap of PbS Quantum Dots. *Appl. Phys. Lett.* **2017**, *111*, 233101.

(16) Blöchl, P. E. Projector Augmented-Wave Method. *Phys. Rev. B: Condens. Matter Mater. Phys.* **1994**, *50*, 17953−17979.

(17) Monkhorst, H. J.; Pack, J. D. Special Points Fro Brillouin-Zone Integretions. *Phys. Rev. B: Solid State* **1976**, *13*, 5188−5192.

(18) Leslie, M.; Gillan, N. J. The Energy and Elastic Dipole Tensor of Defects in Ionic Crystals Calculated by the Supercell Method. *J. Phys. C: Solid State Phys.* **1985**, *18*, 973−982.

(19) Makov, G.; Payne, M. C. Periodic Boundary Conditions in Ab Initio Calculations. *Phys. Rev. B: Condens. Matter Mater. Phys.* **1995**, *51*, 4014−4022.
(20) Baroni, S.; Resta, R. Ab Initio Calculation of the Macroscopic Dielectric Constant in Silicon. *Phys. Rev. B: Condens. Matter Mater. Phys.* **1986**, *33*, 7017−7021.
(21) Lany, S.; Zunger, A. Assessment of Correction Methods for the Band-Gap Problem and for Finite-Size Effects in Supercell Defect Calculations: Case Studies for ZnO and GaAs. *Phys. Rev. B: Condens. Matter Mater. Phys.* **2008**, *78*, 235104.
(22) Lany, S.; Zunger, A. Accurate Prediction of Defect Properties in Density Functional Supercell Calculations. *Model. Simul. Mater. Sci. Eng.* **2009**, *17*, 084002.
(23) Zhang, S.; Northrup, J. Chemical Potential Dependence of Defect Formation Energies In. *Phys. Rev. Lett.* **1991**, *67*, 2339−2342.
(24) Patterson, A. L. The Scherrer Formula for X-Ray Particle Size Determination. *Phys. Rev.* **1939**, *56*, 978−982.
(25) Nesbitt, H. W.; Banerjee, D. Interpretation of XPS Mn (2p) Spectra and Constraints on the of Mn Oxyhydroxides Mechanism of MnO , Precipitation. *Am. Mineral.* **1998**, *83*, 305−315.
(26) Biesinger, M. C.; Payne, B. P.; Grosvenor, A. P.; Lau, L. W. M.; Gerson, A. R.; Smart, R. S. C. Resolving Surface Chemical States in XPS Analysis of First Row Transition Metals, Oxides and Hydroxides: Cr, Mn, Fe, Co and Ni. *Appl. Surf. Sci.* **2011**, *257*, 2717−2730.
(27) Spanjaard, D.; Guillot, C.; Desjonquères, M.-C.; Tréglia, G.; Lecante, J. Surface Core Level Spectroscopy of Transition Metals: A New Tool for the Determination of Their Surface Structure. *Surf. Sci. Rep.* **1985**, *5*, 1−85.
(28) Citrin, P. H.; Wertheim, G. K.; Baer, Y. Core-Level Binding Energy and Density of States from the Surface Atoms of Gold. *Phys. Rev. Lett.* **1978**, *41*, 1425−1428.
(29) Wooten, D.; Ketsman, I.; Xiao, J.; Losovyj, Y. B.; Petrosky, J.; McClory, J.; Burak, Y. V.; Adamiv, V. T.; Dowben, P. A. The Surface Core Level Shift for Lithium at the Surface of Lithium Borate. *Phys. B* **2010**, *405*, 461−464.
(30) Losovyj, Y. B.; Wooten, D.; Santana, J. C.; An, J. M.; Belashchenko, K. D.; Lozova, N.; Petrosky, J.; Sokolov, A.; Tang, J.; Wang, W.; et al. Comparison of N-Type Gd2O3 and Gd-Doped HfO 2. *J. Phys.: Condens. Matter* **2009**, *21*, 045602.
(31) Gupta, R. P.; Sen, S. K. Calculation of Multiplet Structure of Core p -Vacancy Levels. II. *Phys. Rev. B: Solid State* **1975**, *12*, 15−19.
(32) Grosvenor, A. P.; Kobe, B. A.; Biesinger, M. C.; McIntyre, N. S. Investigation of Multiplet Splitting of Fe 2p XPS Spectra and Bonding in Iron Compounds. *Surf. Interface Anal.* **2004**, *36*, 1564−1574.
(33) Lin, T.-C.; Seshadri, G.; Kelber, J. A. A Consistent Method for Quantitative XPS Peak Analysis of Thin Oxide Films on Clean Polycrystalline Iron Surfaces. *Appl. Surf. Sci.* **1997**, *119*, 83−92.
(34) Yamashita, T.; Hayes, P. Analysis of XPS Spectra of Fe2+ and Fe3+ Ions in Oxide Materials. *Appl. Surf. Sci.* **2008**, *254*, 2441−2449.
(35) Cao, S.; Paudel, T. R.; Sinha, K.; Jiang, X.; Wang, W.; Tsymbal, E. Y.; Xu, X.; Dowben, P. A. The Stability and Surface Termination of Hexagonal LuFeO3. *J. Phys.: Condens. Matter* **2015**, *27*, 175004.
(36) Cao, S.; Zhang, X.; Sinha, K.; Wang, W.; Wang, J.; Dowben, P. A.; Xu, X. Phase Separation in LuFeO3 Films. *Appl. Phys. Lett.* **2016**, *108*, 202903.
(37) Beniwal, S.; Zhang, X.; Mu, S.; Naim, A.; Rosa, P.; Chastanet, G.; Létard, J.-F.; Liu, J.; Sterbinsky, G. E.; Arena, D. A.; et al. Surface-Induced Spin State Locking of the [Fe(H2B(Pz)2)2(Bipy)] Spin Crossover Complex. *J. Phys.: Condens. Matter* **2016**, *28*, 206002.
(38) Dowben, P. A.; Sakisaka, Y.; Rhodin, T. N. Angle-Resolved Photoemission from Molecular N2 Adsorbed on Ni(100). *Surf. Sci.* **1984**, *147*, 89−102.
(39) Ortega, J. E.; Himpsel, F. J.; Li, D.; Dowben, P. A. Initial and Final State Contributions of the Core Level Shifts for Gd(0001). *Solid State Commun.* **1994**, *91*, 807−811.
(40) Xiao, J.; Dowben, P. a. The Role of the Interface in the Electronic Structure of Adsorbed Metal(II) (Co, Ni, Cu) Phthalocyanines. *J. Mater. Chem.* **2009**, *19*, 2172−2178.
(41) Xiao, J.; Sokolov, A.; Dowben, P. A. Changing Band Offsets in Copper Phthalocyanine to Copolymer Poly(Vinylidene Fluoride with Trifluoroethylene) Heterojunctions. *Appl. Phys. Lett.* **2007**, *90*, 242907.
(42) Golze, M.; Grunze, M.; Driscoll, R. K.; Hirsch, W. XPS as a Tool to Study the Kinetics and Thermodynamics of Molecular Adsorption: N2 on Ni(110). *Appl. Surf. Sci.* **1980**, *6*, 464−472.
(43) Abo-Namous, S. A.; Andrews, P. T.; Johnson, C. E. Plasmon Loss and Plasmon Gain in Mg-Cd Alloys. *J. Phys. F: Met. Phys.* **1979**, *9*, 61−70.
(44) Unsworth, P.; Evans, J. E.; Weightman, P.; Takahashi, A.; Matthew, J. A. D.; Herd, Q. C. Temperature dependence of the phonon broadening of the Si 2pXPS line. *Phys. Rev. B: Condens. Matter Mater. Phys.* **1996**, *54*, 286−290.
(45) Minnhagen, P. Increased Phonon Broadening of Due to Finite Core-Hole Lifetime. *J. Phys. F: Met. Phys.* **1976**, *6*, 1789−1800.
(46) Citrin, P. H.; Hamann, D. R. Phonon Broadening of X-Ray Photoemission Line Shapes in Solids and Its Independence of Hole State Lifetimes. *Phys. Rev. B: Solid State* **1977**, *15*, 2923−2928.
(47) Feldkamp, L. A.; Davis, L. C. Spin Polarization of the Resonant Two-Hole Bound Sate in Ni Photoemission. *Phys. Rev. Lett.* **1979**, *43*, 151−154.
(48) Dowben, P. A. Metallicity of Thin Films and Overlayers. *Surf. Sci. Rep.* **2000**, *40*, 151−247.
(49) Raz, B.; Gedanken, A.; Even, U.; Jortner, J. Screening of Wannier Exciton States near the Metal-Insulator Transition. *Phys. Rev. Lett.* **1972**, *28*, 1643−1646.
(50) Komesu, T.; Huang, X.; Paudel, T. R.; Losovyj, Y. B.; Zhang, X.; Schwier, E. F.; Kojima, Y.; Zheng, M.; Iwasawa, H.; Shimada, K.; et al. Surface Electronic Structure of Hybrid Organo Lead Bromide Perovskite Single Crystals. *J. Phys. Chem. C* **2016**, *120*, 21710−21715.
(51) Kim, D.; Yang, J.-h.; Hong, J. Ferromagnetism Induced by Zn Vacancy Defect and Lattice Distortion in ZnO. *J. Appl. Phys.* **2009**, *106*, 013908.
(52) Hong, N. H.; Sakai, J.; Brizé, V. Observation of Ferromagnetism at Room Temperature in ZnO Thin Films. *J. Phys.: Condens. Matter* **2007**, *19*, 036219.
(53) Tuomisto, F.; Ranki, V.; Saarinen, K.; Look, D. C. Evidence of the Zn Vacancy Acting as the Dominant Acceptor in N-Type ZnO. *Phys. Rev. Lett.* **2003**, *91*, 205502.
(54) Zhou, S.; Xu, Q.; Potzger, K.; Talut, G.; Grötzschel, R.; Fassbender, J.; Vinnichenko, M.; Grenzer, J.; Helm, M.; Hochmuth, H.; et al. Room Temperature Ferromagnetism in Carbon-Implanted ZnO. *Appl. Phys. Lett.* **2008**, *93*, 232507.
(55) Yan, W.; Sun, Z.; Liu, Q.; Li, Z.; Pan, Z.; Wang, J.; Wei, S.; Wang, D.; Zhou, Y.; Zhang, X. Zn Vacancy Induced Room-Temperature Ferromagnetism in Mn-Doped ZnO. *Appl. Phys. Lett.* **2007**, *91*, 062113.
(56) Xu, Q.; Schmidt, H.; Hartmann, L.; Hochmuth, H.; Lorenz, M.; Setzer, A.; Esquinazi, P.; Meinecke, C.; Grundmann, M. Room Temperature Ferromagnetism in Mn-Doped ZnO Films Mediated by Acceptor Defects. *Appl. Phys. Lett.* **2007**, *91*, 092503.
(57) Proshchenko, V.; Horoz, S.; Tang, J.; Dahnovsky, Y. Room Temperature D0ferromagnetism in ZnS Nanocrystals. *J. Appl. Phys.* **2016**, *119*, 223901.
(58) Göktaş, A.; Mutlu, I. H. Room Temperature Ferromagnetism in Mn-Doped ZnS Nanocrystalline Thin Films Grown by Sol-Gel Dip Coating Process. *J. Sol−Gel Sci. Technol.* **2014**, *69*, 120−129.
(59) Pimachev, A.; Rimal, G.; Nielsen, R. D.; Tang, J.; Dahnovsky, Y. Room Temperature D0 Ferromagnetism in PbS Films: Nonuniform Distribution of Pb Vacancies. *Phys. Chem. Chem. Phys.* **2018**, *20*, 29804−29810.
(60) Yoon, S. D.; Chen, Y.; Yang, A.; Goodrich, T. L.; Zuo, X.; Arena, D. A.; Ziemer, K.; Vittoria, C.; Harris, V. G. Oxygen-Defect-Induced Magnetism to 880 K in Semiconducting Anatase TiO 2-δ Films. *J. Phys.: Condens. Matter* **2006**, *18*, L355−L361.
(61) Hong, N. H.; Sakai, J.; Poirot, N.; Brizé, V. Room-Temperature Ferromagnetism Observed in Undoped Semiconducting and Insulat-

DOI: 10.1021/acs.jpcc.9b06551
J. Phys. Chem. C 2019, 123, 24890−24898

ing Oxide Thin Films. *Phys. Rev. B: Condens. Matter Mater. Phys.* **2006**, *73*, 132404.
(62) Hong, N. H.; Poirot, N.; Sakai, J. Ferromagnetism Observed in Pristine SnO2 Thin Films. *Phys. Rev. B: Condens. Matter Mater. Phys.* **2008**, *77*, 033205.
(63) Venkatesan, M.; Fitzgerald, C. B.; Coey, J. M. D. Unexpected Magnetism in a Dielectric Oxide. *Nature* **2004**, *430*, 630.
(64) Proshchenko, V.; Karanovich, A.; Dahnovsky, Y. Surface-Bulk Model for D0 Ferromagnetism in ZnS Quantum Dots and Wires. *J. Phys. Chem. C* **2016**, *120*, 11253−11261.
(65) Tang, J.-P.; Wang, L.-l.; Luo, H.-J.; Xiao, W.-Z. Magnetic Properties in Zinc-Blende CdS Induced by Cd Vacancies. *Phys. Lett. A* **2013**, *377*, 572−576.
(66) Winterstein, A.; Akamatsu, H.; Möncke, D.; Tanaka, K.; Schmidt, M. A.; Wondraczek, L. Magnetic and Magneto-Optical Quenching in (Mn^{2+}, Sr^{2+}) Metaphosphate Glasses. *Opt. Mater. Express* **2013**, *3*, 184.
(67) Goldenberg, N. Magnetism and Valency: Manganese Compounds. *Trans. Faraday Soc.* **1940**, *36*, 847−854.
(68) N, H.; Elizabeth, S. *Structure and Magnetic Properties of Tb1-XSrxMnO$_3$*, 2015; Vol. *1667*, p 130016.
(69) Wang, Y.; Piao, J.; Xing, G.; Lu, Y.; Ao, Z.; Bao, N.; Ding, J.; Li, S.; Yi, J. Zn Vacancy Induced Ferromagnetism in K Doped ZnO. *J. Mater. Chem. C* **2015**, *3*, 11953−11958.
(70) Wang, Q.; Sun, Q.; Chen, G.; Kawazoe, Y.; Jena, P. Vacancy-Induced Magnetism in ZnO Thin Films and Nanowires. *Phys. Rev. B: Condens. Matter Mater. Phys.* **2008**, *77*, 205411.
(71) Wang, Y.; Luo, X.; Tseng, L.-T.; Ao, Z.; Li, T.; Xing, G.; Bao, N.; Suzukiis, K.; Ding, J.; Li, S.; et al. Ferromagnetism and Crossover of Positive Magnetoresistance to Negative Magnetoresistance in Na-Doped ZnO. *Chem. Mater.* **2015**, *27*, 1285−1291.

DOI: 10.1021/acs.jpcc.9b06551
J. Phys. Chem. C 2019, 123, 24890−24898